Fluid circulation driven by collectively organized metachronal waves in swimming *T. aceti* nematodes

A. C. Quillen,[1,*] A. Peshkov,[1,†] Brato Chakrabarti,[2,‡] Nathan Skerrett,[1,§] Sonia McGaffigan,[1,‖] and Rebeca Zapiach[3,¶]

[1]*Department of Physics and Astronomy, University of Rochester, Rochester, New York 14627, USA*

[2]*Center for Computational Biology, Flatiron Institute, New York, New York 10010, USA*

[3]*Department of Mechanical Engineering, University of Rochester, Rochester, New York 14627, USA*

(Received 9 September 2022; accepted 17 November 2022; published 2 December 2022)

Recent experiments have shown that the nematode *T. aceti* can assemble into collectively undulating groups at the edge of fluid drops. This coordinated state consists of metachronal waves and drives fluid circulation inside the drop. We find that the circulation velocity is about 2 mm/s and nearly half the speed of the metachronal wave. We develop a quasi-two-dimensional hydrodynamics model using the Stokes flow approximation. The periodic motion of the nematodes constitute our moving boundary condition that drives the flow. Our model suggests that large-amplitude excursions of the nematode tails produce the fluid circulation. We discuss the constraints on containers that would enhance fluid motion, which could be used in the future design of on demand flow generating systems.

DOI: 10.1103/PhysRevE.106.064401

I. INTRODUCTION

Turbatrix aceti (*T. aceti*) are a type of freely swimming nematode that have been shown to collectively self-organize at the fluid-air interface to form traveling waves [1,2]. Individual *T. aceti* nematodes, also called vinegar eels, are self-propelled swimmers that continuously consume energy. Thus, a dense suspension of vinegar eels is an example of active matter [3].

Perhaps the most common example of emergent traveling waves is the much studied problem of ciliary carpets. There hydrodynamic interactions between actively beating cilia spontaneously result in the formation of large-scale waves, known as metachronal waves [4]. Such organized waves are critical for the motility of ciliated protists (such as *Paramecium* [5]), mucus clearance in mammalian airways [6,7], and fluid transport in the brain [8].

What makes our model system of vinegar eels unique is that, unlike cilia which are affixed to a cell membrane, these are freely swimming organisms. They fall under a special class of active agents called swarmalators that can self-propel and synchronize their phase of locomotion [9]. It is natural to speculate whether the nematode-produced metachronal wave [1,2] can be harnessed to drive coherent fluid flows. Key to answering this question are quantitative measurements of the emergent flow, and this is the focus of this paper.

The emergence of coherent fluid pumping states has been reported in both experiments and simulations of other wet active matter systems. For example, cytoplasmic streaming in plant cells emerges by microfilament self-organization [10]. With an oil emulsion containing droplets of a highly concentrated aqueous suspension of *Bacillus subtilis*, the bacterial suspension organizes into a single stable circulating vortex, resulting in fluid pumping [11]. Collectively formed vortices or mills in plant-animal worms drive fluid flow [12]. Simulations of tiny swimming particles (microswimmers) show that schools can corral a volume of liquid much larger than the sum of the volumes swept along by each individual [13]. Examples of active-matter-driven pumps include the design of microfluidic devices that can guide and control motility of self-propelled swimmers resulting in directional flows [14–16].

An advantage of studying vinegar eels, compared to many other active systems, is their relatively large size. Vinegar eels are visible by eye and 1–2 mm in length, exceeding the size of flagellates, bacteria, and many types of cells. The soil nematode *Caenorhabditis elegans* (*C. elegans*) belongs to the same order of *Rhabditida* as *Turbatrix aceti* and is widely studied as it is both genomically defined and amenable to genetic manipulation. However, metachronal waves have not been observed in suspensions of *C. elegans* [1].

In analogy to ciliary transport [17], in this paper we seek to understand the relation between the collectively organized traveling waves and the generated fluid flows. We combine experimental observations of dense suspensions of *T. aceti* nematodes with hydrodynamic modeling. The paper is organized as follows. In Sec. II we present our experimental measurements that reveal circulating flow driven by the collective organization of the nematodes in a fluid drop. In Sec. III we compute the flow field using a vertical average for Stokes flow and a moving periodic boundary condition. In Sec. IV A we present experimental observations of the motion of the tails of nematodes that participate in the metachronal wave. The role of the tail motion in influencing the hydrodynamics is explored in Sec. IV B and we speculate about the

*alice.quillen@rochester.edu
†apeshkov@ur.rochester.edu
‡bchakrabarti@flatironinstitute.org
§nskerret@u.rochester.edu
‖smcgaffi@u.rochester.edu
¶rzapiach@u.rochester.edu

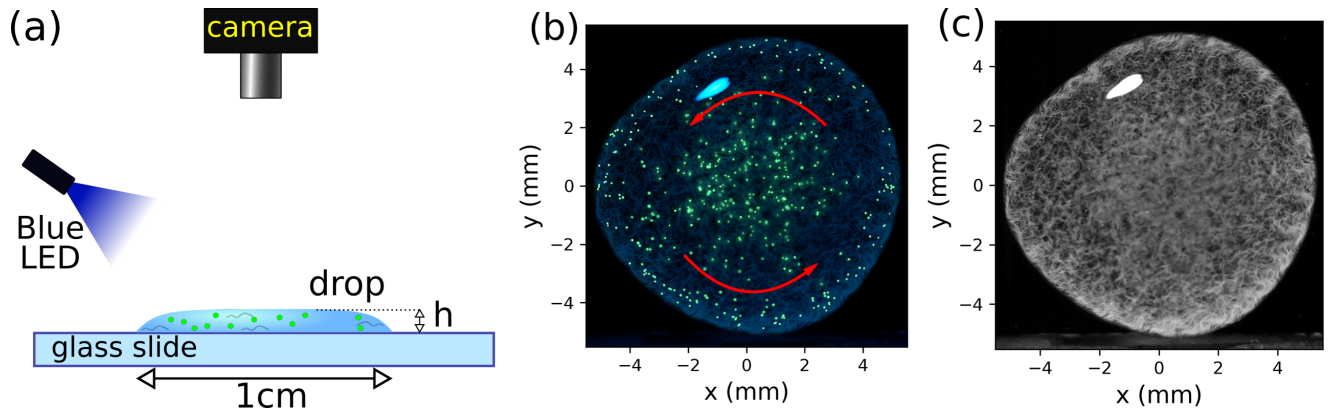

FIG. 1. (a) Illustration of the experimental setup. A dilute drop of vinegar contains swimming nematodes and fluorescent microspheres. It is filmed from above with a video camera. Blue light is absorbed by the microspheres which fluoresce in yellow green. The microspheres are used to track circulation induced by collective motion in the vinegar eel population. (b) Color image from the video which has been annotated to show the direction of circulation. (c) Postprocessed image from the video shows the nematodes at the boundary.

biomechanics of the nematode body motion in Sec. IV C. A summary and discussion follow in Sec. V.

II. EXPERIMENTAL METHODS AND RESULTS

A. Sample preparation

We grow the nematodes in a 1:1 solution of distilled water and food grade apple cider vinegar at approximately 5% concentration. For the experiment, 14 ml of the grow culture containing the nematodes is centrifuged for 3 min at 5000 rpm. This causes the nematodes to form a dense clump at the bottom of the centrifuge tube. We extract 300 μl of this dense solution and mix it with 10 ml of water and 10 μl of a solution containing fluorescent yellow polyethylene microspheres and a Tween 80 biocompatible surfactant. The spheres have a diameter of 63–75 μm and a density of 1.00 g cm^{-3}. The resulting solution is centrifuged again. Afterward 100 μl of the concentrated solution is extracted from the bottom of the centrifuge tube and placed onto a bare glass slide. The resulting droplet that we film for analysis has a diameter of approximately 1 cm and a height $h \approx 1$ mm.

B. Imaging

The experimental setup for imaging is shown in Fig. 1(a) and a video taken with this setup is included as video A in [18]. The fluorescent microsphere markers are used to measure the flow induced by the collective motion of the nematodes. We light the slide with bright blue LEDs, causing the microspheres to fluoresce in yellow green. The drop is filmed in color at 60 frames/s and from above with a Blackmagic Pocket 4K digital camera.

Image frames at a single time from video A in [18] are shown in Figs. 1(b) and 1(c). In Fig. 1(b) we show one of the video frames in color. The microspheres appear green as they fluoresce and the nematodes appear blue because of the LED lighting. To best show the nematodes, we subtract a scaled version of the red frames from the blue ones. The resulting image is converted to grayscale and shown in Fig. 1(c). The nematodes have collected on the boundary and the metachronal wave can be seen in the wavelike features on the outer edge of the drop. Higher-magnification images (see [2], as well as Sec. IV A and video B in [18]) show that the nematode heads are near the boundary and their bodies are oriented at an angle with respect to the boundary so that their tails extend into the circulating fluid. The bright oval on the top left of the images is a reflection from the lights used to illuminate the drop and can be ignored.

C. Tracking particles

The fluorescent microspheres were tracked using the software package TRACKPY [19], which implements in PYTHON the Crocker-Grier algorithm for finding and tracking single-particle trajectories [20]. The microsphere tracers are of sufficiently low concentration that we do not expect them to significantly affect the nematode behavior.

In Fig. 2(a) we show tracks traced by fluorescent microspheres during 1 s of video A [18] on top of one of the video frames. In Fig. 2(b) we show velocity vectors computed from these tracks. In red and with thicker arrows we show average velocities computed by fitting a line to the trajectory of each microsphere in 1 s of video. This averages over several oscillations of the metachronal wave to better show fluid circulation. Circulation of the microspheres can also be seen directly from viewing video A [18]. Instantaneous velocities are computed from the positions of the particles in the first two frames of video A [18]. In Fig. 2(b) the instantaneous velocities are shown with thin brown arrows.

Using a polar coordinate system with the origin at the center of the drop, we measure the azimuthal and radial velocity components v_θ and v_r, respectively, for each tracked microsphere. In Fig. 3(a) the microsphere azimuthal components of the average velocity (using 1 s of video) are shown as a function of distance d from the outer drop boundary. As indicated by the dotted line in the figure, the circulation velocity decays as a function of distance from the boundary and goes to zero at the center of the drop. The black dotted line in Fig. 3(a) shows the curve $v_\theta(d) = u_c e^{-(d-d_0)/h_s}$ with the parameters u_c and d_0 and decay length h_s. The offset d_0 is used to describe a peak distance where circulation is highest and u_c gives the peak circulation velocity. Such an exponential

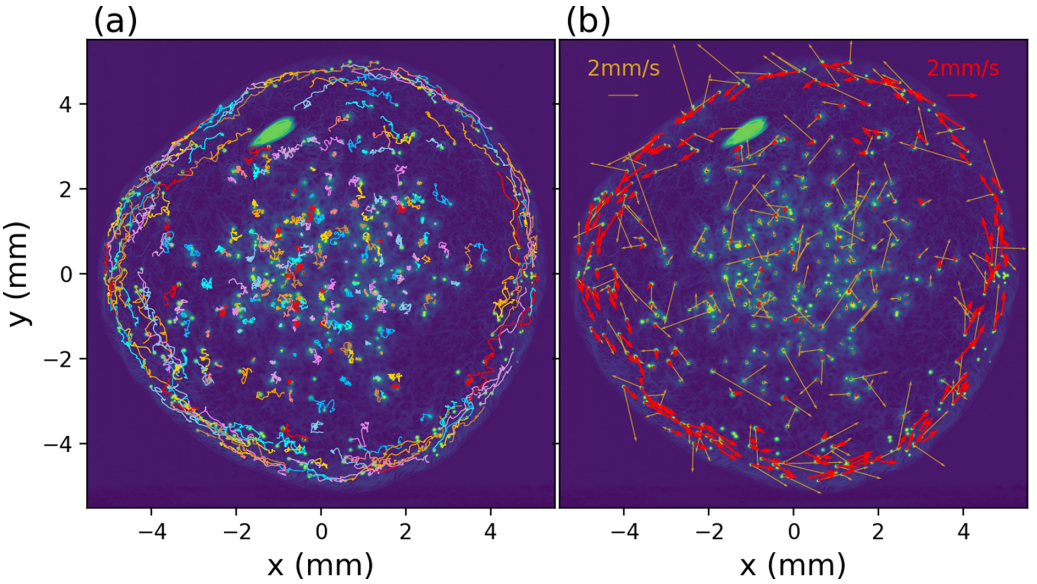

FIG. 2. (a) Tracks of individual fluorescent microspheres from video A in [18]. The spheres were tracked using 60 video frames during 1 s of video. The tracks are shown on top of the first video frame from the video. (b) Velocities of the fluorescent spheres averaged over 1 s of video are shown with red arrows on top of the first video frame in the sequence. The thinner brown arrows show instantaneous velocities of the same spheres computed from positions in two consecutive video frames.

decay results from hydrodynamic-screening-caused flow near boundaries [21–23]. In the following section we will show that the decay length h_s is consistent with hydrodynamic screening in a shallow drop.

In Figs. 3(b) and 3(c) we plot the instantaneous azimuthal and radial velocity components, respectively, as a function of distance from the drop edge. The exponential curve from Fig. 3(a) is overlayed on Fig. 3(b) for comparison and illustrates that the instantaneous velocity can be larger than the time-averaged circulation speed. The velocities we measure for the microspheres can exceed the forward swim speed of the nematodes that are involved in the wave. The nematodes forming the wave advance along the border at a much slower speed, approximately 0.1 mm/s slower than both the metachronal wave and the average azimuthal velocity [1,2], highlighting the emergence of large-scale coherent transport through collective self-organization. The instantaneous velocities are higher than the averaged azimuthal velocity component because of oscillations associated with the metachronal wave and perturbations caused by close interactions with individual nematodes.

D. Metachronal wave measurements

We characterize the kinematics of the emerging metachronal wave. We measure the metachronal wave frequency f_{MW} with a cross-correlation technique, as described by Quillen *et al.* [2]. We compute the product of two image frames separated by an interval of time and then sum the pixel values in the entire product image. The peaks in the sum occur at multiples of the metachronal wave period. We similarly measure the metachronal wavelength λ_{MW}, by rotating an individual frame about the center of the drop, multiplying it by the original frame, and summing over the product image. Peaks in the sum occur at rotations that are the metachronal wavelength divided by the drop radius. Errors in these quantities are estimated from the strength and widths of the peaks in these sums. These measurements are summarized in Table I. We also list a range of values for the peak averaged azimuthal or tangential speed u_c and decay length h_s consistent with the average azimuthal velocities shown in Fig. 3(a).

The wavelength of the metachronal wave is $\lambda_{\mathrm{MW}} \sim 1$ mm, similar to that of our previous measurements [2]. The metachronal wave frequency is $f_{\mathrm{MW}} \approx 5.45$ Hz, which is within the 4–8 Hz range measured in similar experiments [1]. Together these give a metachronal wave velocity $v_{\mathrm{MW}} = \lambda_{\mathrm{MW}} f_{\mathrm{MW}} \approx 5.1$ mm/s. Near the collective wave, the microspheres have a mean averaged azimuthal or tangential velocity component of about $u_c \sim 2$ mm/s. The ratio of the microsphere mean azimuthal velocity component to the metachronal wave speed is about $u_c/v_{\mathrm{MW}} \sim \frac{2}{5}$.

III. HYDRODYNAMIC THEORY FOR COHERENT FLOWS

To understand the underlying mechanics of the coherent transport driven by the metachronal waves, we build a

TABLE I. Measurements.

Parameter	Value
radius of drop R_d	5.25 mm
volume of drop V_{drop}	100 μl
metachronal frequency f_{MW}	5.45 ± 0.16 Hz
metachronal wavelength λ_{MW}	0.93 ± 0.09 mm
metachronal wave speed V_{MW}	5.1 ± 0.5 mm/s
speed of average flow u_c	2 ± 1 mm/s
exponential decay length of average flow h_s	0.7 ± 0.2 mm

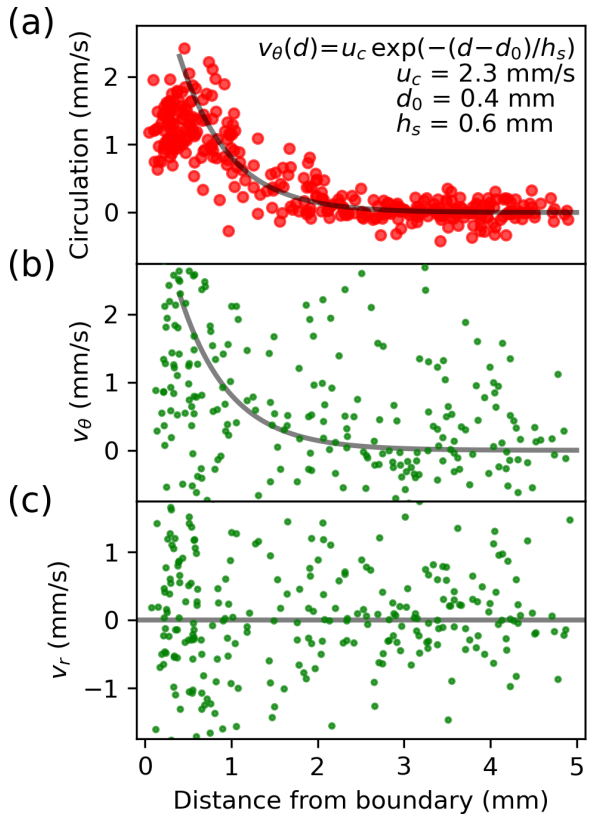

FIG. 3. Microsphere velocities. (a) Average azimuthal velocity component v_θ of tracked microspheres as a function of distance from the outer drop edge. The gray line shows an exponentially decaying function with function and parameters in the legend. (b) Instantaneous azimuthal velocity component of microspheres as a function of distance from the drop outer edge. The gray line shows the same exponentially decaying function as in (a). (c) Microsphere instantaneous radial velocity component as a function of distance from the drop outer edge. The gray line shows a velocity of zero.

quasi-two-dimensional (quasi-2D) hydrodynamic model for the fluid flow. With a flow velocity of 1 mm/s, a length scale of 1 mm, and dynamic viscosity of water $\nu \sim 10^{-6}$ m^2 s$^{-1} = 1$ mm^2 s^{-1}, the Reynolds number is about 1, so inertia could be important in the velocity field. Nevertheless, we use a model that is appropriate in the Stokes or low-Reynolds-number limit.

A. Hele-Shaw approximation for the quasi-2D flow

We consider a three-dimensional incompressible flow field in the drop $\mathbf{U} = \{U, V, W\}$. In the limit of low Reynolds number, the evolution of the flow field is governed by the incompressible Stokes flow equations

$$\nabla \cdot \mathbf{U} = 0, \tag{1}$$

$$-\frac{1}{\rho}\nabla p + \nu\nabla^2\mathbf{U} = \mathbf{0}, \tag{2}$$

where p is the pressure and ν is the kinematic viscosity of the fluid. The velocity field $\mathbf{U}$ is a function of $(\mathbf{x}_\parallel, z)$, where $\mathbf{x}_\parallel = \{x, y\}$ spans the plane on which the drop resides and the height of the drop $h(\mathbf{x}_\parallel)$ and $0 \leqslant z \leqslant h(\mathbf{x}_\parallel)$. The characteristic drop thickness $h \sim 1$ mm is smaller than the typical drop radius of $R \sim 5$ mm. This natural scale separation allows us to invoke the lubrication approximation [24]. Scaling $\mathbf{x}_\parallel \sim R$ and $z \sim h$, we find $W \sim \{U, V\}h/R$. In the limit $h/R \ll 1$ the vertical velocity $W = 0$ to the leading order and $\partial_z p = 0$ (see, e.g., [12]). The smallness of the aspect ratio h/R can be exploited to separate the wall-normal dependence (i.e., in the direction z) of the velocity field from its in-plane averaged value, as is done in classical Hele-Shaw problems [25]. For this purpose, we adopt the ansatz for the velocity field

$$\mathbf{U}(\mathbf{x}_\parallel, z) = \mathbf{u}(\mathbf{x}_\parallel) f(z) \tag{3}$$

(following [12]), where $f(z)$ is a single scalar function which describes the velocity profile over the height of the cell and $\mathbf{u}(\mathbf{x}_\parallel) = u\hat{\mathbf{x}} + v\hat{\mathbf{y}}$ is a 2D depth averaged velocity field defined as

$$\mathbf{u}(\mathbf{x}_\parallel) = \frac{1}{h}\int_0^h \mathbf{U}\, dz. \tag{4}$$

The ansatz of Eq. (3) is reasonable because the vertical velocity vanishes to the leading order of the problem. The form of $f(z)$ depends on the boundary conditions. For flow in the droplet with a free top interface and no-slip bottom surface we take

$$f(z) = \frac{3}{2}\left[1 - \left(1 - \frac{z}{h}\right)^2\right]. \tag{5}$$

On the other hand, for flow between two flat plates with no-slip boundary conditions we could use $f(z) = 6(z/h - z^2/h^2)$. The ansatz of Eq. (3) along with the definition for $\mathbf{u}$ gives

$$\partial_{zz}\mathbf{U} = -\alpha_z\frac{\mathbf{u}}{h^2}, \tag{6}$$

where $\alpha_z = 3$ for a free interface [consistent with Eq. (5)] and $\alpha_z = 12$ for flow between two no-slip boundaries. In our above formulation we have ignored curvature effects of the drop height near the boundaries. This amounts to assuming that the surface tension effects and the forces from the nematodes in determining the drop shape are negligible (for a discussion of these effects see [1]).

We average Eqs. (1) and (2) over depth to obtain the quasi-2D approximation for the evolution of the velocity field

$$\nabla_\parallel \cdot \mathbf{u} = 0, \tag{7}$$

$$-\frac{1}{\rho}\nabla_\parallel p + \nu\left[\nabla_\parallel^2 - \frac{\alpha_z}{h^2}\right]\mathbf{u} = \mathbf{0}, \tag{8}$$

where $\nabla_\parallel = \partial_x\hat{\mathbf{x}} + \partial_y\hat{\mathbf{y}}$ is the 2D gradient and $\nabla_\parallel^2$ is the associated 2D Laplacian. The above set of equations differs from the two-dimensional incompressible Stokes equation by the additional dissipative term $-\alpha_z/h^2$ which accounts for the average friction force between the surface and the droplet interface. By omitting the term $\nabla_\parallel^2\mathbf{u}$ we would obtain the so-called Darcy approximation of the Navier-Stokes equation, which is often used to model flows in porous media and viscous fingering in Hele-Shaw cells and describes potential flow. In our case, the flow need not be in general a potential flow [26,27]. The above set of equations is often termed the Brinkman correction to Hele-Shaw flows [12,25]. It is worth

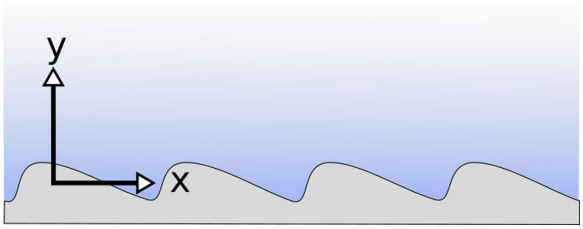

FIG. 4. Coordinate directions. The boundary is on the bottom and the direction to the center of the drop is upward. The metachronal wave travels to the right. We ignore the curvature of the drop boundary. Here the drop is viewed from above.

pointing out that the Green's function associated with the full Stokes equation is nontrivial [28] and involves the use of the method of images to calculate the flow field [12,21,28] (see [29] on the validity of approximation). One advantage of the 2D Brinkman approximation is that it circumvents this challenge and allows us to compute tractable solutions in a spatially periodic domain, as we discuss next.

Since the depth-averaged velocity $\mathbf{u}$ acts like a two-dimensional incompressible fluid, we can describe the two-dimensional flow with a stream function $\psi(\mathbf{x}_\parallel)$, where

$$(u, v) = (\partial_y \psi, -\partial_x \psi). \tag{9}$$

The vorticity ω is related to the Laplacian of the stream function

$$\omega = \partial_x v - \partial_y u = -\partial_{xx}\psi - \partial_{yy}\psi = -\nabla_\parallel^2 \psi. \tag{10}$$

Upon taking the curl of Eq. (8) we obtain the evolution of the vorticity as

$$\nabla_\parallel^2 \omega = \frac{\alpha_z}{h^2}\omega. \tag{11}$$

With negative α_z, this is known as the homogeneous Helmholtz equation, and with positive α_z, it is known as the homogeneous screened Poisson equation.

As the exponential decay length h_s is smaller than the drop radius R_d, with $h_s/R_d \approx 0.13$ we can neglect the curvature of the drop edge. We set our x direction along the azimuthal direction of the drop and the y direction is aligned with radius from the drop center and is increasing with distance from the drop edge (see Fig. 4). Since the flow field is driven by the motion of the nematode tails, we expect the solutions to be periodic along x over a metachronal wavelength. For positive α_z, a general solution of Eq. (11) that is periodic in x, with period $\lambda_{\mathrm{MW}} = 2\pi/k_{\mathrm{MW}}$, and decays at larger y has the stream function

$$\begin{aligned}\psi(x, y) = a_0 e^{-y/h_s} + \sum_{j=1}^{\infty} \{&[a_{cj}\cos(jk_{\mathrm{MW}}x) + a_{sj}\sin(jk_{\mathrm{MW}}x)] \\ &\times e^{-\beta_j jk_{\mathrm{MW}}y}[b_{cj}\cos(jk_{\mathrm{MW}}x) \\ &+ b_{sj}\sin(jk_{\mathrm{MW}}x)]e^{-jk_{\mathrm{MW}}y}\},\end{aligned} \tag{12}$$

with coefficients a_0, a_{cj}, a_{sj}, b_{cj}, and b_{sj}, where

$$\beta_j \equiv \sqrt{1 + \frac{\alpha_z}{(jk_{\mathrm{MW}}h)^2}}. \tag{13}$$

The characteristic length scale for the exponential decay associated with the constant circulating term with coefficient a_0 is

$$h_s \equiv \frac{h}{\sqrt{\alpha_z}}. \tag{14}$$

The terms with coefficients b_{cj} and b_{sj} have zero vorticity as they satisfy Laplace's equation $\nabla_\parallel^2 \psi = 0$.

The term proportional to α_z in Eq. (8) gives rise to hydrodynamic screening with an exponential decay length of $h_s = h/\sqrt{\alpha_z}$ typical in the Brinkman correction [30]. With a drop thickness of about $h \sim 1$ mm and $\alpha_z = 3$, consistent with a fixed no-slip lower boundary and stress-free upper interface, the decay length $h_s \sim 0.6$ mm. This is consistent with the decay length measured in the induced circulation in Sec. II.

B. Metachronal wave boundary condition

The nematodes engaged in the metachronal wave are densely packed. Their heads are near the outer edge of the boundary and the tails touch moving fluid. This suggests that the coherent circulating flow is driven by the motion of the tails of the nematodes involved in the wave. To incorporate this in our model, we develop a kinematic description of the tail motion. We assume that the tails act like a moving, continuous no-slip boundary for the fluid flow. The trajectory of each point on the boundary is described by a periodic function associated with the oscillatory motion in the wave. The metachronal wave gives a delay between the trajectories of neighboring boundary points.

Neglecting curvature of the drop edge, the boundary is spatially periodic in x with wavelength λ_{MW} and with metachronal wave traveling in the positive x direction with velocity V_{MW}. We use the coordinate $s \in [0, \lambda_{\mathrm{MW}})$ to describe positions along the boundary. The trajectory of a material point at $s = 0$ is described by a displacement function $\boldsymbol{\delta}_0(t)$ which is temporally periodic with frequency f_{MW}. Due to the propagating traveling wave, a point on the boundary that is displaced horizontally from the reference point at $s = 0$ undergoes the same trajectory but delayed in time. With $\mathbf{x}_b = (x_b, y_b)$, points on the boundary evolve as

$$\mathbf{x}_b(s, t) = \boldsymbol{\delta}_0\left(t - \frac{s}{V_{\mathrm{MW}}}\right) + s\hat{\mathbf{x}} + \mathbf{x}_m. \tag{15}$$

In the above description, the boundary is a one-dimensional space curve that is described by a displacement vector function $\boldsymbol{\delta}_0(t - s/V_{\mathrm{MW}})$. This yields a wave traveling with the metachronal wave velocity V_{MW}. The constant $\mathbf{x}_m$ sets the position of the boundary at $s = t = 0$. The velocity of points on the boundary

$$\mathbf{V}_b(s, t) = \frac{d}{dt}\left[\boldsymbol{\delta}_0\left(t - \frac{s}{V_{\mathrm{MW}}}\right)\right]. \tag{16}$$

The no-slip boundary condition for the fluid velocity implies that

$$\mathbf{V}_b(s, t) = \mathbf{u}[\mathbf{x}_b(s, t)]. \tag{17}$$

TABLE II. Parameters for flow models.

Parameter	Value
metachronal wavelength $\lambda_{\rm MW}$	1 mm
metachronal frequency $f_{\rm MW}$	5 Hz
screening parameter α_z	3
drop thickness h	1 mm
screening length $h_s = \frac{h}{\sqrt{\alpha_z}}$	0.6 mm

C. Finding a flow field consistent with the velocity on the boundary

Once a set of positions on the boundary and the velocities of these positions are specified, we try to obtain a two-dimensional fluid flow field consistent with the boundary condition. For this we use a minimization algorithm to find the coefficients in the solution of the stream function in Eq. (12), as illustrated below.

Using Eq. (17) for the boundary condition and integrating over the boundary, we construct a non-negative function

$$g(\boldsymbol{\delta}_0, \psi) = \frac{1}{L_b}\int_0^{L_b} |\mathbf{V}_b(s) - \mathbf{u}(s)|^2 ds, \tag{18}$$

where L_b is the length of the boundary corresponding to a single wavelength of the metachronal wave. The above function is zero for a velocity field $\mathbf{u}(\mathbf{x}_\parallel)$ derived from a stream function $\psi(\mathbf{x}_\parallel)$ using Eq. (9) that is consistent with the velocity boundary condition described by the displacement function $\boldsymbol{\delta}_0(t)$. We use a multivariate minimization algorithm to minimize this function for different values of the coefficients in Eq. (12). For the present problem we retain $j = 20$ Fourier modes for the stream function, which results in 81 free parameters. To carry out the minimization we use the Nelder-Mead simplex method available through PYTHON's SCIPY.OPTIMIZE package. The quality of the result is measured by computing the standard deviation σ_v of the difference between the flow velocity and boundary velocity integrated on the boundary. This is equivalent to the square root of the minimization function $\sigma_v = \sqrt{g(\boldsymbol{\delta}_0, \psi)}$. Once the fitting is done, the coefficient a_0 of the stream function allows us to compute and characterize the average flow speed in the model at $y = y_m$ as

$$u_c(y_m) = -\frac{a_0}{h_s} e^{-y_m/h_s}. \tag{19}$$

The key parameters for our boundary model are listed in Table II. We choose $\alpha_z = 3$, corresponding to a fixed lower boundary and a stress-free upper boundary as discussed in Sec. III A. We take the drop thickness $h = 1$ mm, which yields a screening length for the solution, $h_s = 0.6$ mm, consistent with our experimental measurements.

D. Role of different boundary motions in fluid circulation

Motivated by our prior work on a phase oscillator model for the collective motion [2], we consider the velocity field that would arise from a boundary where each point has a small amplitude of oscillation compared to the metachronal wavelength $\lambda_{\rm MW}$. We describe the displacement vector of points on the boundary with the function

$$\boldsymbol{\delta}_0(t) = A_b \cos(\omega_{\rm MW} t)\hat{\mathbf{y}} + [B_b \cos(\omega_{\rm MW} t) - C_b \sin(\omega_{\rm MW} t)]\hat{\mathbf{x}}, \tag{20}$$

with $\omega_{\rm MW} = 2\pi f_{\rm MW}$ and three constant coefficients A_b, B_b, and C_b. We include only three terms because we can adjust the phase of the wave to remove a term that is proportional to $\sin(\omega_{\rm MW} t)\hat{\mathbf{y}}$. Positions on the boundary $\mathbf{x}_b(s,t)$ are then generated from $\boldsymbol{\delta}_0(t)$ using Eq. (15). To compute the average flow velocity [via Eq. (19)] we take y_m to be the distance between the mean y component of $\boldsymbol{\delta}_0(t)$ and the drop edge.

TABLE III. Oscillating boundary models.

Parameter	Model A	Model B	Tail trajectory
amplitude (mm) A_b	0.10	0.10	
amplitude (mm) B_b	−0.05	−0.07	
amplitude (mm) C_b	0.0	0.10	
circulation or flow (mm/s) $u_c(y_m)$	−0.6	1.9	2.6
viscous dissipation per $\lambda_{\rm MW}$ (pW)	70	86	830
power in circulation	1%	9%	2%

Depending on the choice of the constants in Eq. (20), we obtain qualitatively different models for the boundary motion. We explore two models, referred to as model A and model B, with properties summarized in Table III. Model A has $C_b = 0$ and each particle on the boundary moves back and forth along a line segment. This model is similar to the phase oscillator model [2] developed previously where the points on the nematode bodies move back and forth, but at an angle with respect to the outer drop edge. Model B has $C_b \neq 0$ and each particle on the boundary particles has a loop-shaped trajectory. Model B is inspired by geometric approaches for describing flows near oscillating boundaries [31–33]. In this setting a loop trajectory on a surface is described with two infinitesimal operators that do not commute [31], resulting in a flow velocity that is described via a curvature known as the Stokes curvature [32,33]. Figures 5(a) and 5(c) display the boundary position at a given time instant for the two different boundary models, with the arrows indicating the instantaneous velocity of the material points. The blue line on the left shows the trajectory of a single point on the boundary over one oscillation period.

The associated velocity fields for these two boundary models are depicted in Figs. 5(b) and 5(d) and their circulation speeds are listed in Table III. Interestingly, model A, with back and forth oscillation of boundary material points, yields a small circulation speed u_c and predicts the incorrect direction for circulation with $u_c < 0$. In contrast, model B provides a circulation speed that is consistent with what we observed experimentally. The computed solution captures features of the experimental flow field, including the back and forth motion associated with the metachronal wave. Both model A and B flow fields have a rms velocity difference of $\sigma_v = 0.3$ mm/s between the flow and boundary [the square root of the minimization function in Eq. (18)].

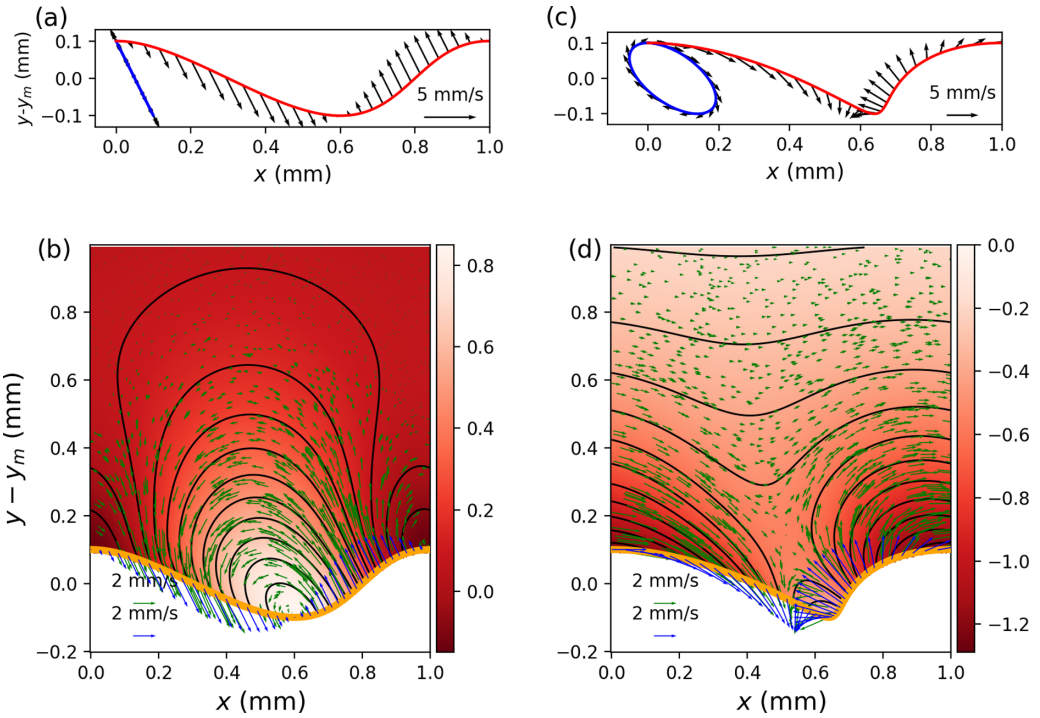

FIG. 5. (a) In blue we show the position of a single point on the boundary during a full oscillation period for a sinusoidal oscillating boundary referred to as model A and with parameters listed in Table III. In red we show the boundary at single moment in time. Velocity vectors are shown with black arrows. (b) Velocity field for model A that was found by minimizing the function of Eq. (18) over the boundary shown in (a). The stream function is shown as a red image and with black contours. Velocity vectors in the fluid are shown with green arrows. The velocity vectors on the boundary are shown with blue arrows. (c) Similar to (a) but for the sinusoidal oscillating boundary model B. (d) Associated velocity field for model B.

E. Energetics of the flow

It is natural to ask how much energy is required to maintain these streaming flows or what fraction of the energy injected by the nematode body motion is used by the coherent flows. To answer this we estimate the viscous dissipation from the velocity fields computed in Figs. 5(b) and 5(d) (see the Appendix for details). Using viscosity $\mu = 0.9$ mPa s, we find that the estimated dissipation rate is about 80 pW per wavelength for both models of the boundary motion (see Table III). With about 20 vinegar eels per metachronal wavelength, this corresponds to 4 pW per vinegar eel. Remarkably, we find that for model B, only about 9% of this power goes into maintaining fluid circulation, corresponding to the constant or a_0 term in the stream function given in Eq. (12) (see Table III). The remainder of the power goes into oscillatory fluid motion.

IV. ROLE OF TAIL MOTION IN DRIVING FLUID FLOW

The computed flow models for the oscillating boundaries suggest that elliptical trajectories for points on a boundary are necessary to drive the level of circulation in the fluid that we saw in video A in [18]. As the nematode heads are trapped at the drop edge, the motion is primarily imparted by the nematode tails moving within the circulating fluid. To better understand how the circulation is driven, we examine the behavior of tails of the nematodes involved in the metachronal wave.

A. Observed tail trajectories

To make accurate measurements of the eel tails, we use the 10× magnification and high-speed videography (1057 frames/s) described previously in [2] (see video B in [18]). For a few nematode tails, we mark their positions on every frame using the software package IMAGEJ. The resulting tail trajectories are shown in Fig. 6 and they are also marked in video B in [18]. In Fig. 6(a), tail-tip positions are plotted for about an oscillation period with thick colored lines on top of a grayscale image from video B. The tail-tip velocities are shown with small arrows. Thin colored segments highlight tangent directions for the tail. In Fig. 6(b) we display smoothed versions of the same six tail-tip trajectories. The trajectories are shifted horizontally so that their mean x positions are the same. The similarity between the six trajectories gives us confidence that the measured trajectories are associated with the collective motion.

Based on our previous study of phase oscillator models for the formation of the metachronal wave [2], we had expected the nematode tails to remain near the bodies of other nematodes that are participating in the metachronal wave. The phase oscillator model assumed that material points on nematode bodies are oscillating back and forth with an amplitude of about 0.1 mm and do not involve large-amplitude elliptical motion. However, as shown in Fig. 6 and seen in video B in [18], the tracked tail-tip trajectories are not ellipses but figure-8 shapes. Excursions away from the drop edge (in the y direction in Fig. 6) are about 0.8 mm, which is almost as large

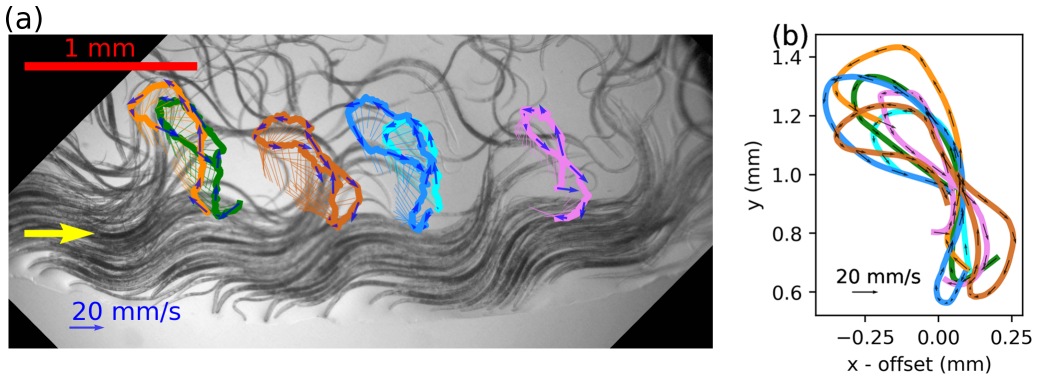

FIG. 6. Tail trajectories as seen in a higher-magnification high-speed video. (a) Six nematode tail tips are tracked and plotted with a thick line. Each tail tip is plotted with a different color. Arrows show the velocity of the tail tip. Thin colored segments show tangent directions for the tail at a subset of times with each segment ending at a tail-tip location. The underlying grayscale image shows a frame from the high-speed video (video B in [18]). A scale bar is shown in red in the top left corner. The yellow arrow shows that the metachronal wave travels to the right. The heads of vinegar eels involved in the metachronal wave are located at the bottom of the image, near the edge of the drop. (b) Smoothed versions of the same six tracked tail trajectories. Horizontal x positions have been shifted so that the mean position is near zero. Vertical y positions give the distance from the drop edge.

as the metachronal wavelength of 1 mm and exceeds the back and forth motion of the rest of the nematode bodies and their heads. The tail tips extend well outside the region near the boundary where the nematodes are densely packed and their velocities can be as high as approximately 10 mm/s.

We find that some tails could not be tracked for a whole period because they go out of focus during part of the video. We note that video B is of a shallow drop, with a depth about half that of the drop shown in video A in [18]. The shallower depth facilitates viewing individual nematodes, as they are less likely to go in and out of focus, an issue at higher magnification. However, as discussed in Sec. III A, a shallower drop depth reduces the screening length h_s. We have no reason to suspect that the depth affects the motion of nematodes participating in the metachronal wave, though the drop shape can influence whether metachronal wave can form [1].

B. Flow field computed from tail trajectories

We proceed to compute the fluid flow resulting from the observed tail trajectories. We use a single tail trajectory to generate a boundary from a sequence of tails undergoing the metachronal wave using Eq. (15). In Fig. 7(a) we show the trajectory of the rightmost tail of Fig. 6(a) with a dotted line. The associated wave boundary is shown with a solid thick line. The generated boundary shows that the tail would overlap with neighboring nematodes at different times, which is indeed confirmed from the examination of video B in [18] that highlights the large tail-tip excursions. To generate a boundary, we choose the rightmost trajectory, shown in pink in Fig. 6(a), because it has the least oscillatory motion in the x direction and provides the least overlap. Reduced overlap in the boundary condition is desirable since it is unphysical to have different fluid velocities at a single point in our 2D fluid model. Using the boundary shown in Fig. 7(a), we generate an associated two-dimensional fluid flow with the method described in Sec. III C. The flow is shown Fig. 7(b). The circulation [computed from Eq. (19)] and viscous dissipation rate for this flow model are listed in the rightmost column of Table III. The quality of fit, estimated from Eq. (18), gives a rms of $\sigma_v \sim 2$ mm/s, which is poorer than for the flows associated with models A and B. The higher value is probably due to the higher velocities on the boundary and the unphysical overlap region.

The average flow velocity $u_c = 2.6$ mm/s, for the flow shown in Fig. 7(b), is sufficiently high to be consistent with the experimental values reported in Fig. 3(a). Integrating horizontally, we find that the standard deviation of the v velocity component at $y = 0.4$ is 1.6 mm/s. This is comparable to the standard deviation, 1.1 mm/s, of the instantaneous radial velocity component we measured and showed in Fig. 3(c). Interestingly, we find that the power required to drive the flow is about 40 pW per nematode in the wave with only 2% of this power being used for fluid circulation. This estimated power is about 10 times higher than the 3 pW power estimated power for propulsion of *C. elegans* [34], suggesting that vinegar eels expend more energy while they are in the metachronal wave than they would while freely swimming. We speculate that this could be because (i) tail trajectories for nematodes in the metachronal (extending a maximum distance about 0.8 mm peak to peak) are larger than those of a freely swimming eel [which are about 0.3 mm peak to peak (see the right-hand side of Fig. 1 in [2])], (ii) flow velocities may be overestimated because of overlaps in the tail trajectories, and (iii) due to confinement, nematodes involved in the metachronal wave would expend part of their energy pushing against each other. The power required to drive both the metachronal wave and the associated circulation per nematode could be up to an order of magnitude higher than that expended while freely swimming. Improved hydrodynamic modeling would be needed to better estimate the power required to drive the flow and modeling taking into account steric interactions would be needed to estimate the power dissipated within the nematode bodies.

C. Mechanical model for a single tail motion

Our analysis of the nematode tail trajectories in the preceding section revealed a characteristic figure-8 shape for

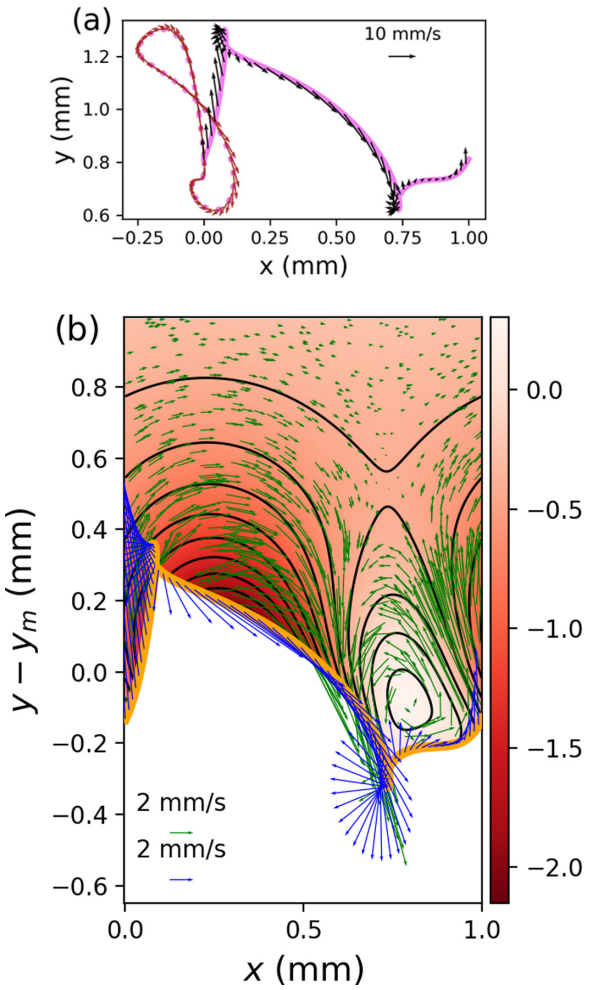

FIG. 7. (a) Trajectory of the rightmost tail in Fig. 6 shown as a pink dotted line on the left, after smoothing. Points on the trajectory are shifted and delayed using Eq. (15) to give the pink solid line, which shows the boundary position at a single moment during propagation of the metachronal wave. Arrows show velocity vectors of points on the boundary. (b) Flow field associated with a boundary that is approximated by the tail-tip trajectories. The boundary condition is given by points and velocities on the solid line in (a). The colormap shows the stream function and its contours are plotted with black lines. The thick orange line shows the boundary. Blue vectors show velocities on the boundary. Green vectors show fluid velocities. The y axis shows $y - y_m$, where y_m is approximately the mean y position of a boundary point.

the tail tips. We seek to develop a mechanical model that sheds light on such an emergent pattern. We build a simplified model for the backbone of an isolated nematode. We model the centerline dynamics of an individual nematode as a planar, inextensible Euler elastica with bending rigidity B. The centerline is parametrized by arclength s and identified by a Lagrangian marker $\mathbf{x}(s,t)$. Following [35], the actuation in the nematode that produces periodic traveling undulation is modeled using a preferred time-dependent curvature given by

$$\kappa_0(s,t) = \frac{As}{L}\sin(k_w s - 2\pi\Omega_0 t). \tag{21}$$

Here k_w is the wave number of the target curvature, A is the amplitude, and Ω_0 is the frequency. We consider the nematode head at $s = 0$ to be fixed in space, as the heads of nematodes participating in the metachronal wave do not move very far (see Fig. 5 in [2]). The tail at $s = L$ is both force- and moment-free. Since the vinegar eel is a slender object, we model its hydrodynamics using local slender body theory [36,37], which relates the viscous forces $\mathbf{f}_v(s)$ per unit length to the centerline velocity as

$$8\pi\mu\partial_t\mathbf{x}(s,t) = -\mathcal{L}[\mathbf{f}_v]. \tag{22}$$

Here μ is the fluid viscosity and $\mathcal{L}$ is the local mobility operator that accounts for drag anisotropy along the body and is given by

$$\mathcal{L}[\mathbf{f}_v](s) = \left[\frac{1}{\xi_\perp}\hat{\mathbf{n}}(s)\hat{\mathbf{n}}(s) + \frac{1}{\xi_\parallel}\hat{\mathbf{t}}(s)\hat{\mathbf{t}}(s)\right]\cdot\mathbf{f}_v(s), \tag{23}$$

where $\xi_\perp = (2-c)^{-1}$ and $\xi_\parallel = -(2c)^{-1}$ are resistance coefficients in the normal and tangential directions. For a slender body, the coefficient c is assumed to be negative and small. In the above expression, $\{\hat{\mathbf{t}}(s), \hat{\mathbf{n}}(s)\}$ are the tangent and normal vectors along the centerline, respectively. The elastic forces are related to the viscous forces following the force and moment balance equations

$$\mathbf{f}_v + \partial_s\mathbf{F} = \mathbf{0}, \tag{24}$$

$$\mathbf{M}_s + \partial_s\mathbf{x}\times\mathbf{F} = \mathbf{0}. \tag{25}$$

Here the $\mathbf{F}$ are the elastic contact forces of an inextensible rod and $\mathbf{M}$ is the bending moment of the filament given by $\mathbf{M}(s) = -B[\kappa(s,t) - \kappa_0(s,t)]\mathbf{x}_s\times\mathbf{x}_{ss}$ (here $\mathbf{x}_s$ refers to the derivative $\partial_s\mathbf{x}$). Scaling length by L and time with the relaxation time $\tau = 8\pi\mu L^4/B$ of an elastic filament, the nematode body shapes are governed by three dimensionless numbers: (i) A/L, which sets the amplitude of the target curvature; (ii) $k_w L$, which sets the dimensionless wave number; and (iii) $W = \Omega_0\tau$, the worm number [35], which compares the frequency of wave propagation to the elastic relaxation time of the nematode body. Using $L = 2$ mm, $B = 10^{-14}$ N m^2 [38], and $f_0 = 2\pi\Omega_0 = 5$ Hz, we obtain $W \approx 40$. We solve the coupled set of partial differential equations. numerically as outlined in [37,39].

The shapes of the nematode body and the tail trajectories at $\mathbf{x}(s = L)$ are outlined in Fig. 8 and reveal the natural emergence of the figure-8 trajectory shape at the tail tip. A figure-8-shaped tail-tip trajectory can be seen in the similar model of an elastic filament [examine Fig. 3(b) in [40]]. Figure 8 also shows that the amplitude of motion reaches a maximum near the tail tip, which is consistent with observations of both freely swimming nematodes and those participating in the metachronal wave. However, these simulations do not give tail amplitudes as large as we see in either setting. We compare the largest distance between any two points in the tail trajectory. This distance is 0.8 mm for the tails tracked in Fig. 6(b), 0.26 mm for the freely swimming eel shown in Fig. 1 in [2], but only 0.16 mm in the model tail trajectory shown in Fig. 8(b). The body shapes in Fig. 8(a) have decreasing wavelength near the tail tip, opposite to what we observe, suggesting that the tails are stiffer or remain

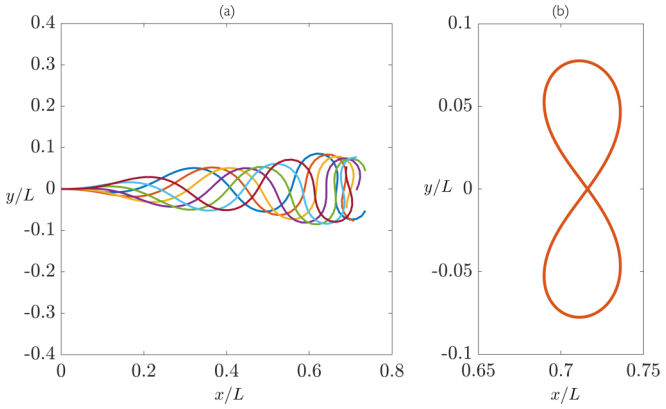

FIG. 8. (a) Shape of an isolated nematode as computed from the preferred-curvature model. (b) Characteristic figure-8 shape of the tail tips emerging from the inextensibility of the nematode body.

straighter than the rest of the nematode bodies. When body curvature propagates down a nematode body, as required for locomotion (see, e.g., [41]), we find that a natural outcome is a figure-8-shaped tail-tip trajectory. However, a more complex model than explored here, including steric interactions and possibly proprioceptive feedback [41,42], would be needed to better match the observed body shapes.

V. SUMMARY AND DISCUSSION

Using fluorescent microspheres, we have measured the circulation velocity of flow in a 1-cm-diam and 1-mm-deep drop that is driven by collective motion in a concentration of swimming *T. aceti* nematodes, which are commonly called vinegar eels. The mean circulation velocity is about 2 mm/s and located within 1 mm of the outer edge of the drop. We found that the ratio of circulating flow velocity to metachronal wave speed is about $\frac{2}{5}$ and decays rapidly as a function of distance from the outer drop edge.

Perturbative models [43–45] for causing steady flow by wavelike ripples on a surface have been developed for three-dimensional flows in the Stokes flow or low-Reynolds-number limit. These predict that the driven flow depends on the square of the amplitude of surface perturbations in units of the wavelength times the surface wave speed. This scaling suggests that the ratio of flow speed to wave speed should be low. In this context, the ratio of $2/5$ for the ratio of circulation speed to metachronal wave speed that we measured in the dilute vinegar drop is unexpectedly high.

Unlike the planar sheet model [43,44] where the fluid lies in an infinite three-dimensional half space, our system is shallow, with a fixed lower boundary (the slide that our drop lies on) and a free upper boundary (the drop surface). We take into account the shallow drop depth by integrating the velocity vertically as a function of depth. Depth-averaged velocities give a two-dimensional hydrodynamic model. Neglecting variation of the vertical velocity profiles and drop thickness on horizontal position, the fluid obeys the homogeneous screened Poisson equation, typical of Hele-Shaw flow [12,25].

Using the trajectory of a single nematode tail, we constructed a boundary condition for the metachronal wave by delaying the tail-tip trajectory at neighboring positions. This model gives us the velocity and location of particles along a moving one-dimensional boundary. With a general solution to the 2D homogeneous screened Poisson equation that decays at large distances from the boundary and using an optimization routine, we find the stream function that minimizes the difference between the fluid velocity and particle velocities on the boundary. The screening in the screened Poisson equation is sensitive to the drop depth, with shallower drops having circulating flows that decay more rapidly as a function of distance from the moving boundary than flows in deeper drops. We find that the circulation or streaming velocity is sensitive to the boundary particle trajectory shape, with ellipse trajectories more effective than linear trajectories at driving circulation.

We had expected to find that the tails of nematodes participating in the metachronal wave undergo ellipse trajectories. However, upon examination, we found that the tails of the nematodes undergoing collective motion have figure-8 trajectories and undergo large 0.8-mm excursions away from the drop edge. These are about twice as large as tail motion exhibited by a freely swimming nematode or most of the nematode body that is participating in the metachronal wave.

To probe the mechanical origins of the tail motion we constructed a simple preferred curvature model for an isolated nematode. This model captures the characteristic figure-8 shape of the tail and shows that this shape is naturally caused by a curvature wave propagating down an elastic body. While this model captures the characteristic figure-8 shape of the tail and an increase in amplitude toward the tail tip, the simulated results are not in great agreement for an isolated nematode. This can be possibly due to subtle structural features associated within the nematode such as varying cross-sectional width along its backbone and variations in how such structural features alter the internal force generation. The associated biomechanics is left for future consideration. Understanding collective effects poses another set of challenges in modeling. For example, in contrast with the experimental measurements for nematodes participating in the metachronal wave, our simple mechanical model does not predict large-amplitude oscillations of the tail tip. Since hydrodynamic interactions are screened, we believe that such emergent dynamics of the nematode tails could be associated with local steric interactions. Our prior work suggested that steric interactions were required for metachronal wave formation in the vinegar eel system and caused the waves traveling down the nematode bodies to deviate from a pure sinusoidal function [2]. Recently, it has been proposed that steric interactions alone can lead to the emergence of collective behaviors in arrays of cilia and alter their isolated waveforms [46]. The potential role of such effects remains to be explored.

A flow model generated with a boundary generated from the observed tail motion exhibits sufficient circulation to be consistent with the circulation we observed experimentally. The flow model suggests that the motion of the vinegar eel tails is important for driving fluid circulation.

The high ratio of circulation flow speed to metachronal wave speed that we measured suggests that systems of nematodes could be engineered to drive flows. What type of container would best give fluid circulation? Bordertaxis of the nematodes should be facilitated; otherwise the nematodes

will not enter a collective state giving a metachronal wave. The container edge where the eels would be corralled could be shallow (less than 1 mm thick) or beveled, similar to the contact angle caused by surface tension in a drop [with contact angle below 70° (see [1])]. The top surface could be covered, rather than open, though this would affect the screening length scale. We assumed an open surface giving $\alpha_z \sim 3$ and a screening exponential length $h_s = h/\sqrt{\alpha_z}$ [as in Eq. (14)], where h is the depth of the container. With a fixed upper boundary (for an enclosed container) we would expect $\alpha_z \sim 12$. A container twice as deep would be needed to give the same screening length in a closed container as one with an open surface. A beveled edge might be the best compromise as it might corral the eels, facilitating collective motion while simultaneously allowing a larger screening exponential decay length for the driven flow. Large-amplitude motion in the nematode tails would help drive circulation, so the distance between outer and inner container edges should be at least a few millimeters.

We observed nematode bodies overlapping other nematodes in our high-magnification video and there are numerous nematodes that are not engaged in the collective motion. Our 2D flow and boundary model neglects motion of overlapping nematodes and those that do not participate in the collective motion. Extending the fidelity and capability of the hydrodynamic modeling is challenging but would improve understanding of the relation between collective motion in a dense concentration of oscillating swimming organisms and associated flows resulting from their collective motion.

ACKNOWLEDGMENTS

This material was based upon work supported in part by National Science Foundation Grant No. PHY-1757062 and National Science Foundation Grant No. DMR-1809318. We thank Michael J. Shelley and Adam Lamson for helpful discussions and suggestions. We thank the Flatiron Institute, Center for Computational Biology for their hospitality. We thank Maya Parada for many interesting discussions on the subject of designing and manufacturing containers for the vinegar eels.

APPENDIX: COMPUTING VISCOUS DISSIPATION

The viscous dissipation rate in an incompressible flow depends on the traceless part of the velocity gradient

$$\sigma_{ij} = \tfrac{1}{2}\left(\partial_{x_j} u_i + \partial_{x_i} u_j\right). \tag{A1}$$

The viscous dissipation rate per unit volume

$$\dot{\epsilon} = \mu \,\mathrm{tr}\sigma^2 = \mu \sum_{ij} (\sigma_{ij})^2, \tag{A2}$$

where the dynamic viscosity $\mu = \rho\nu$ and ν is the kinematic viscosity.

We integrate over z to find the viscous dissipation rate per unit area. It is useful to compute dimensionless constants that depend on the assumed form for the velocity field as a function of depth

$$\bar{f} = \frac{1}{h}\int_0^h f(z)dz, \tag{A3}$$

$$c_0 = \frac{1}{h}\int_0^h f(z)^2 dz, \tag{A4}$$

$$c_1 = h\int_0^h f'(z)^2 dz. \tag{A5}$$

The full three-dimensional velocity field (U, V, W) is related to the vertically averaged two-dimensional velocity field (u, v) with

$$\begin{aligned} U(x,y,z,t) &= \frac{1}{\bar{f}} u(x,y,t) f(z), \\ V(x,y,z,t) &= \frac{1}{\bar{f}} v(x,y,t) f(z), \\ W(x,y,z,t) &= 0. \end{aligned} \tag{A6}$$

From U, V, and W we compute the different components of the velocity gradient tensor in terms of the stream function.

$$\begin{aligned} \sigma_{xx} &= \partial_x U = \frac{f(z)}{\bar{f}}\partial_x u = \frac{f(z)}{\bar{f}}\partial_{xy}\psi, \\ \sigma_{yy} &= \partial_x V = \frac{f(z)}{\bar{f}} f(z)\partial_y v = -\frac{f(z)}{\bar{f}}\partial_{xy}\psi, \\ \sigma_{zz} &= \partial_z W = 0, \\ \sigma_{xz} &= \frac{1}{2}(\partial_x W + \partial_z U) = \frac{f'(z)}{2\bar{f}} u = \frac{f'(z)}{2\bar{f}}\partial_y\psi, \\ \sigma_{yz} &= \frac{1}{2}(\partial_y W + \partial_z V) = \frac{f'(z)}{2\bar{f}} v = -\frac{f'(z)}{2\bar{f}}\partial_x\psi, \\ \sigma_{xy} &= \frac{1}{2}\partial_x V + \partial_y U) = \frac{f(z)}{2\bar{f}}(\partial_x v + \partial_y u) \\ &= \frac{f(z)}{2\bar{f}}(-\partial_{xx}\psi + \partial_{yy}\psi). \end{aligned} \tag{A7}$$

We integrate the squares of the components of the velocity gradient over depth

$$\begin{aligned} \int_0^h dz\,\sigma_{xx}^2 &= \frac{\int_0^h f(z)^2 dz}{(\bar{f})^2}(\partial_{xy}\psi)^2 = \frac{hc_0}{(\bar{f})^2}(\partial_{xy}\psi)^2, \\ \int_0^h dz\,\sigma_{yy}^2 &= \frac{hc_0}{(\bar{f})^2}(\partial_{xy}\psi)^2, \\ \int_0^h dz\,\sigma_{zz}^2 &= 0, \\ \int_0^h dz\,\sigma_{xy}^2 &= \frac{\int_0^h f(z)^2 dz}{(\bar{f})^2}\frac{1}{4}(\partial_{yy}\psi - \partial_{xx}\psi)^2 \\ &= \frac{hc_0}{(\bar{f})^2}\frac{1}{4}(\partial_{yy}\psi - \partial_{xx}\psi)^2, \\ \int_0^h dz\,\sigma_{xz}^2 &= \frac{\int_0^h f'(z)^2 dz}{(\bar{f})^2}\frac{1}{4}(\partial_y\psi)^2 \\ &= \frac{c_1}{h(\bar{f})^2}\frac{1}{4}(\partial_y\psi)^2, \\ \int_0^h dz\,\sigma_{yz}^2 &= \frac{c_1}{h(\bar{f})^2}\frac{1}{4}(\partial_x\psi)^2. \end{aligned} \tag{A8}$$

In terms of the stream function, the viscous dissipation rate per unit area is

$$\dot{e}_A(x,y) = \int_0^h dz\, \dot{\epsilon}(x,y,z)$$
$$= \mu h \left[\frac{c_0}{(\bar{f})^2} \left(2(\partial_{xy}\psi)^2 + \frac{1}{2}(\partial_{yy}\psi - \partial_{xx}\psi)^2 \right) + \frac{c_1}{2h^2(\bar{f})^2}[(\partial_y\psi)^2 + (\partial_x\psi)^2] \right]. \quad \text{(A9)}$$

Using $f(z)$ from Eq. (5), corresponding to a fixed base and free surface, and with Eq. (A5), we find $\bar{f} = \frac{2}{3}$, $c_0 = \frac{8}{15}$, $c_1 = \frac{4}{3}$, $c_0/(\bar{f})^2 = 1.2$, and $c_1/(\bar{f})^2 = 3$, which are used in Eq. (A9). To estimate the viscous dissipation rate, we integrate the dissipation rate per unit area with Eq. (A9), over an area with x ranging from 0 to λ_{MW} and y ranging from the boundary to $y = y_m + \lambda_{MW}$, where y_m [defined in Eq. (15)] is approximately the mean y value for the boundary.

[1] A. Peshkov, S. McGaffigan, and A. C. Quillen, Soft Matter **18**, 1174 (2022).
[2] A. C. Quillen, A. Peshkov, E. Wright, and S. McGaffigan, Phys. Rev. E **104**, 014412 (2021).
[3] M. C. Marchetti, J. F. Joanny, S. Ramaswamy, T. B. Liverpool, J. Prost, M. Rao, and R. A. Simha, Rev. Mod. Phys. **85**, 1143 (2013).
[4] B. Chakrabarti, S. Furthauer, and M. J. Shelley, Proc. Natl. Acad. Sci. USA **119**, e2113539119 (2022).
[5] S. L. Tamm, J. Cell Biol. **55**, 250 (1972).
[6] M. A. Sleigh, J. R. Blake, and N. Liron, Am. Rev. Resp. Dis. **137**, 726 (1988).
[7] B. A. Afzelius, J. Pathol. **204**, 470 (2004).
[8] R. Faubel, C. Westendorf, E. Bodenschatz, and G. Eichele, Science **353**, 176 (2016).
[9] K. P. O'Keeffe, H. Hong, and S. H. Strogatz, Nat. Commun. **8**, 1504 (2017).
[10] F. G. Woodhouse and R. E. Goldstein, Proc. Natl. Acad. Sci. USA **110**, 14132 (2013).
[11] H. Wioland, F. G. Woodhouse, J. Dunkel, J. O. Kessler, and R. E. Goldstein, Phys. Rev. Lett. **110**, 268102 (2013).
[12] G. T. Fortune, A. Worley, A. B. Sendova-Franks, N. R. Franks, K. C. Leptos, E. Lauga, and R. E. Goldstein, J. Fluid Mech. **914**, A20 (2021).
[13] C. Jin, Y. Chen, C. C. Maass, and A. J. T. M. Mathijssen, Phys. Rev. Lett. **127**, 088006 (2021).
[14] M. S. Davies Wykes, X. Zhong, J. Tong, T. Adachi, Y. Liu, L. Ristroph, M. D. Ward, M. J. Shelley, and J. Zhang, Soft Matter **13**, 4681 (2017).
[15] P. Galajda, J. Keymer, P. Chaikin, and R. Austin, J. Bacteriol. **189**, 8704 (2007).
[16] A. Guidobaldi, Y. Jeyaram, I. Berdakin, V. V. Moshchalkov, C. A. Condat, V. I. Marconi, L. Giojalas, and A. V. Silhanek, Phys. Rev. E **89**, 032720 (2014).
[17] L. Xu and Y. Jiang, Cells **8**, 736 (2019).
[18] See Supplemental Material at http://link.aps.org/supplemental/10.1103/PhysRevE.106.064401 for video A, which is a 60-frame/s video of a drop containing vinegar eels (*T. aceti*) and fluorescent particles, showing circulation, and video B, a high-speed 1057-frame/s video of vinegar eels (*T. aceti*) at high concentration seen under the microscope, in which the positions of nematode tails are marked with colored line segments.
[19] D. Allan, T. Caswell, N. Keim, and C. van der Wel, Trackpy v0.3.2, https://doi.org/10.5281/zenodo.60550.
[20] J. C. Crocker and D. G. Grier, J. Colloid Interf. Sci. **179**, 298 (1996).
[21] N. Liron and S. Mochon, J. Eng. Math. **10**, 287 (1976).
[22] M. P. Brenner, Phys. Fluids **11**, 754 (1999).
[23] B. Cui, H. Diamant, and B. Lin, Phys. Rev. Lett. **89**, 188302 (2002).
[24] G. K. Batchelor, *An Introduction to Fluid Dynamics* (Cambridge University Press, Cambridge, 2000).
[25] J. Zeng, Y. C. Yortsos, and D. Salin, Phys. Fluids **15**, 3829 (2003).
[26] W. Boos and A. Thess, J. Fluid Mech. **352**, 305 (1997).
[27] J. W. M. Bush, J. Fluid Mech. **352**, 283 (1997).
[28] A. J. T. M. Mathijssen, A. Doostmohammadi, J. M. Yeomans, and T. N. Shendruk, J. Fluid Mech. **806**, 35 (2016).
[29] G. T. Fortune, Ph.D. thesis, University of Cambridge, 2022.
[30] H. C. Brinkman, Flow Turbul. Combust. **1**, 27 (1949).
[31] E. Purcell, Am. J. Phys. **45**, 3 (1977).
[32] A. Shapere and F. Wilczek, J. Fluid Mech. **198**, 557 (1989).
[33] K. M. Ehlers and J. Koiller, Reg. Chaotic Dyn. **16**, 623 (2011).
[34] J. Sznitman, X. Shen, R. Sznitman, and P. E. Arratia, Phys. Fluids **22**, 121901 (2010).
[35] T. Majmudar, E. E. Keaveny, J. Zhang, and M. J. Shelley, J. R. Soc. Interface **9**, 1809 (2012).
[36] J. B. Keller and S. I. Rubinow, J. Fluid Mech. **75**, 705 (1976).
[37] A.-K. Tornberg and M. J. Shelley, J. Comput. Phys. **196**, 8 (2004).
[38] M. Backholm, W. S. Ryu, and K. Dalnoki-Veress, Proc. Natl. Acad. Sci. USA **110**, 4528 (2013).
[39] B. Chakrabarti and D. Saintillan, Phys. Rev. Fluids **4**, 043102 (2019).
[40] G. D. Canio, E. Lauga, and R. E. Goldstein, J. R. Soc. Interface **14**, 20170491 (2017).
[41] Q. Wen, M. D. Po, E. Hulme, S. Chen, X. Liu, S. W. Kwok, M. Gershow, A. M. Leifer, V. Butler, C. Fang-Yen *et al.*, Neuron **76**, 750 (2012).
[42] Z. Hao, W. Zhou, and N. Gravish, Adv. Robot. **36**, 654 (2022).
[43] G. I. Taylor, Proc. R. Soc. London Ser. A **209**, 447 (1951).
[44] C. Brennan, J. Fluid Mech. **65**, 799 (1974).
[45] J. Koiller, K. Ehlers, and R. Montgomery, J. Nonlinear Sci. **6**, 507 (1996).
[46] R. Chelakkot, M. F. Hagan, and A. Gopinath, Soft Matter **17**, 1091 (2021).